Citation for final published version:

Chang, Zhou, Ren, Wenqing, Wang, Yucheng, Zhang, Jiawei, Liu, Xiaoteng and Xu, Chenxi 2022. A highly co-tolerant anode pt/ti3c2tx-cnt hybrid catalysts for pemfc. Electrocatalysis 14 , pp. 1-8. 10.1007/s12678-022-00768-w

Publishers page: http://dx.doi.org/10.1007/s12678-022-00768-w

A Highly CO-Tolerant Anode Pt/$Ti_3C_2T_x$-CNT Hybrid Catalysts for PEMFC

Zhou Chang[1] · Wenqing Ren[1] · Yucheng Wang[2] · Jiawei Zhang[1] · Xiaoteng Liu[2] · Chenxi Xu[1]

Accepted: 7 August 2022 / Published online: 11 August 2022

Abstract

Carbon monoxide (CO) is extremely poisonous to the Pt catalyst resulting in the available reaction surface reduction and fuel cell performance degradation. Therefore, the reform of natural gas or other hydrocarbons is avoided to be used as the CO is inevitable. CO -tolerant catalysts are required to overcome this bottleneck. Herein, MXene (Ti-$_3C_2T_x$) and carbon nanotube (CNT) hybrid materials are used as the catalytic support to load Pt nanoparticles (NPs) to achieve the anode catalyst for proton-exchange- membrane fuel cell (PEMFC). The Pt/$Ti_3C_2T_x$-CNT catalyst performs higher hydrogen oxidation reaction (HOR) activities and stability compared with the Pt/C catalysts, and the peak power density of PEMFC based on the Pt/ $Ti_3C_2T_x$ -CNT catalyst achieves 0.86 W cm-$^{-2}$ with H-$_2$/air and 1.6 W cm-$^{-2}$ with H-$_2$/O_2. Furthermore, the Pt/$Ti_3C_2T_x$ -CNT catalyst exhibits superior electrocatalyst activity and remarkable CO-tolerant performance, which could be attributed to the metal-support interactions between Pt nanoparticles and Ti-$_3C_2T_x$-CNT hybrid supports.

Keywords CO-tolerant anode · Hybrid catalytic support · Hydrogen oxidation reaction · Metal-support interactions

Introduction

PEMFC is attractive energy storage equipment for vehicles and other applications because of its high energy efficiency and being environmentally friendly [1, 2]. Hydrocarbons and other liquid fuels (for example, methanol) store a lot of energy [3, 4]. Nowadays, the majority of hydrogen pro-duction comes from the steam reforming of natural gas or other hydrocarbons, which makes hydrogen at a lower cost [5]. However, one problem associated with the reformer is the incomplete reaction resulting in inevitable amounts of carbon monoxide (CO) [6]. CO is extremely poisonous to the Pt catalyst because of easier absorption of CO to Pt surface rather than H-$_2$, which will result in a reduction of activ-ity area and degradation of the fuel cell performance [7–9]. There are many significant efforts have been made to over-come the CO poisoning problem; one approach is Pt-based alloy to fabricate CO-tolerant bimetallic electrocatalysts (PtM, where M = Fe, Ni, Co, Mo, Ru, Sn), [10–17] that the non-noble metals improve the CO tolerance of bimetallic electrocatalysts through the electronic effect and bifunctional or oxyphilic effect (accelerating the removal of adsorbed CO by supplying species containing oxygen) [18–20]. On the other hand, the application of metal-support interactions rep-resents a promising strategy to perfectly solve the problem of catalyst poisoning problem, which not only improves the catalyst activity and stability but also alters the electronic properties of metal and thus weakens the metal-CO interac-tion [21].

Metal oxides are the main support for metal-support interactions with metal NPs [22, 23]. However, the poor electronic conductivity of metal oxides restricts their application as catalyst support for PEMFC. MXene, a two -dimensional (2D) material, has attracted great attention as catalyst supports due to its kinetic-favorable layered nanostructure, high conductivity, and good surface reactivity [24–29]. Recently, Li et al. [30] reported a platinum nanoparticle catalyst supported on -Nb_2CT_x MXene for water–gas shift reaction, which exhibited weaker CO adsorption than monometal-lic platinum due to the formation of a Pt–Nb surface alloy. Moreover, MXene as the support of metal catalyst (Pt, Pb, Co, Cu) can significantly improve CO oxidation reaction even at a lower temperature [31–33]. Unfortunately, two-dimensional MXene sheets demonstrated would suffer from

---

✉\ Chenxi Xu
\ xuchenxi@hfut.edu.cn

[1]\ School of Materials Science and Engineering, Hefei University of Technology, Hefei, Anhui 230009, People's Republic of China

[2]\ Faculty of Engineering and Environment, Northumbria University, Newcastle upon Tyne, UK

aggregation and restacking due to van der Waals interactions and hydrogen bonds. However, the combination of MXene nanosheets and carbon nanomaterials to design MXene-carbon hybrid support is a considerable approach to preventing restacking of MXene nanosheets and improving electrochemical performance [34, 35]. Herein, Pt is loaded on $Ti_3C_2T_x$-CNT hybrid support by microwave reduction. This configuration enhanced the reaction activity and stability because of the synergistic effect between Pt and $Ti_3C_2T_x$ -CNT. The Pt/$Ti_3C_2T_x$-CNT electrocatalysts demonstrate a much better CO tolerance than the Pt/C catalyst.

Experimental Section

Synthesis of $Ti_3C_2T_x$ MXene

The preparation of Ti-$3C_2T_x$ nanosheets was carried out as follows [36]: 0.8 g LiF was injected into 10 ml 9 M HCl solution with stirring at 20 °C for 5 min, and then 0.5 g Ti_3AlC_2 was added into the solution with 24 h magnetically stirring at 35 °C. The precipitates were rinsed with deionized water several times until the pH was around 7. Finally, the collected supernatant was collected and vacuum dried.

Synthesis of $Ti_3C_2T_x$-CNT Hybrid Support

$Ti_3C_2T_x$-CNT hybrid support was prepared by a self-assembly process. A total of 100 -ml CNT aqueous (1 mg ml-$^{-1}$) and 100-ml CTAB aqueous (2 mg ml-$^{-1}$) were ultrasonically mixed for 2 h in ambient conditions to fabricate CTAB-CNT, and then CTAB-CNT solution (1 mg ml-$^{-1}$) was added to $Ti_3C_2T_x$ suspension (1 mg ml-$^{-1}$).

Synthesis of Pt/Ti_3C_2Tx-CNT Catalyst

Pt/$Ti_3C_2T_x$-CNT catalyst was prepared by a microwave-assisted polyol reduction method as shown in Scheme S1. Fifty milligrams of Ti-$3C_2T_x$-CNT hybrid support and 1.24 ml of -$H_2PtCl_6 \cdot 6H_2O$ aqueous (40 mg ml-$^{-1}$) were mixed with 50 ml of ethylene glycol solution in a custom-built flask with 2 h of magnetically stirring and adjusting the mixture pH to 10. Finally, the flask was placed in a microwave oven and heated to 160 °C at a power of 500 W for 5 min and filtering precipitates with enough deionized water. After being dried at 60 °C in a vacuum oven overnight, the Pt/$Ti_3C_2T_x$-CNT catalyst sample was collected.

Characterizations

X-ray diffraction (XRD) patterns were examined by X-ray diffraction (XRD, Philips X'Pert Pro diffractometer) with a CuKα X-ray source (λ = 1.5405 Å). Raman patterns were characterized using a HR Evolution Microscopic confocal laser Raman spectrometer. X-ray photoelectron spectroscopy (XPS) data were recorded using an ESCALAB250Xi model. The morphologies of the materials were obtained by JEM1400FLASH and high-resolution transmission electron microscopy (HRTEM). The Pt loading amount on the CNT modified MXene was measured by Agilent 5110 ICP-OES plasma spectrometer, and the Pt loading amount in the measured Pt/$Ti_3C_2T_X$-CNT is 20%.

Electrochemical Measurement

Electrochemical test was under a three-electrode system (working electrode: a glassy carbon rotating disk electrode (area: 0.1963 -cm^2); reference electrode: Ag/AgCl electrode; counter electrode: graphite rod), and the electrochemical experiments were tested in 0.1 M HClO-$_4$ solution (the reversible hydrogen electrode potential is calculated according to E(RHE) = E(Ag/AgCl) +0.0591 * pH +0.197). The working electrode ink was prepared through dissolving 20% Pt/$Ti_3C_2T_x$- CNT and 20%Pt/C in solution (500 μL of deionized water: 450 μL of isopropanol: 50 μL of 5 wt% Nafion solution), and 18 μl catalyst ink was loaded onto the glassy carbon electrode (the Pt loading was 0.092 mg cm-$^{-2}$). The electrochemical surface areas (ECSA) were calculated by the following equation:

$$ECSA_{Pt} = \frac{\frac{S_H}{v}}{0.21\,\mathrm{mC\ cm^{-2}}\ M_{pt}} \quad (1)$$

where S_H is the integrated area of hydrogen desorption peak or hydrogen adsorption peak of the CV, v is for the scanning speed of the CV, and M_{pt} represents the loading mass of Pt on the WE.

CV, LSV, and CO-stripping measurements were worked in 0.1 M -$HClO_4$ solution. CV was measured between 0 and 1.2 V (vs. RHE) at a scan rate of 50 mV -s^{-1}, and LSV was measured at the potential range of −0.1–0.6 V (vs. RHE) with 10mV s^{-1} and 1600 rpm. The catalysts in the electrolyte solution were saturated with CO at 0.1 V (vs. RHE) for 30 min and purged with -N_2 to remove excess CO from the solution for CO stripping. Accelerated stability tests of the Pt/$Ti_3C_2T_X$-CNT catalysts and the commercial Pt/C catalysts were carried out by a consecutive sweep from 0 to 1.2 V at 50mV s^{-1} for 1000 potential cycles in a 0.1 M -$HClO_4$ solution.

Fuel Cell Performance Test The catalyst ink was obtained by mixing commercial 20 wt% Pt/C or 20 wt% Pt/$Ti_3C_2T_x$-CNT catalysts for the anode and commercial 60 wt% Pt/C catalyst for the cathode, respectively. The homogeneous ink was sprayed to the surface of a 5 -cm^2 membrane by ultrasonic spraying. The Pt loadings of cathode and anode were 0.3mg cm^{-2} and 0.1 mg cm-$^{-2}$, respectively. H-$_2$ or a mixture of H- $_2$ with CO and Air/O$_2$ were fed into the cell at flow rates of 150 -cm^3 min^{-1} and 300 -cm^3 min^{-1} (air) or 150 cm^3 min^{-1} (O$_2$), respectively. For the CO-tolerance test, the current density of 0.8 A -cm^{-2} was supplied constantly, and the drop in the voltage was recorded.

Results and Discussions

The XRD of Pt/$Ti_3C_2T_X$ -CNT catalysts is exhibited in Fig. 1a. A characteristic peak of -Ti_3C_2T $_X$ left shift from 9.66 to 6.74° was observed, which indicates the increased interlayer space because of the successful etching and intercalation. The diffraction peaks of Pt at 39.96°, 46.37°, and 67.77° corresponded to (111), (200), and (220), respectively. These results demonstrated that Pt/Ti_3C_2 T_X-CNT had been successfully synthesized. Meanwhile, the disappearance of peak (002) of Ti-$_3C_2T_X$ in Pt/$Ti_3C_2T_X$-CNT represents the incorporation of CNT, which led to an increased interplanar spacing of the MXene flakes when the hybrid support was achieved. All catalysts exhibit obvious peaks at 1360 cm-$^{-1}$ (D band) and 1580 cm-$^{-1}$ (G band) in Raman spectra of the Pt/$Ti_3C_2T_X$-CNT and Pt/C catalysts as shown in Fig. 1b. The Pt/$Ti_3C_2T_X$-CNT catalyst showed a higher I_D/I_G ratio, which indicates the Pt/$Ti_3C_2T_X$- CNT catalyst had a higher degree of graph-ite domain or defects, with a better load capacity of $Ti_3C_2T_X$-CNT hybrid support. The XPS spectra in Fig. 1c reveal the binding energy of C 1 s (284 eV) and Pt 4f (75 eV) in the Pt/C, and the XPS survey of the Pt/Ti_3 C_2T_X-CNT catalyst presented the elements of Pt 4f, C 1 s, Ti 2p and O 1 s with binding energies of 74 eV, 284 eV, 459 eV,

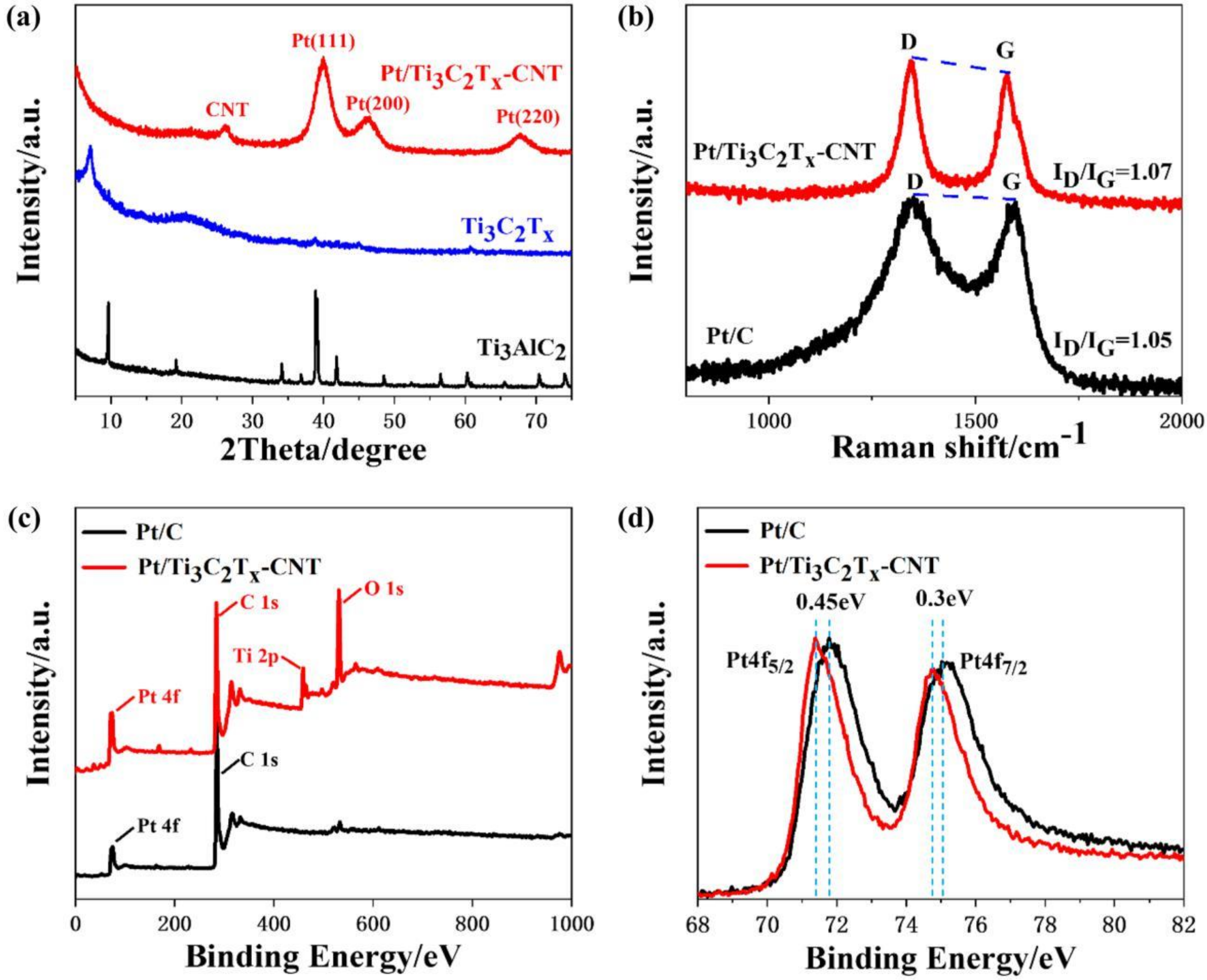

Fig. 1 **a** XRD patterns of Pt/$Ti_3C_2T_X$-CNT, $Ti_3C_2T_X$, and Ti-$_3AlC_2$; **b** Raman spectra of and Pt/C; **c** XPS spectra of Pt/$Ti_3C_2T_X$-CNT and Pt/C; and **d** Pt 4f regions of Pt/C and Pt 4f regions of Pt/C and Pt/$Ti_3C_2T_X$-CNT

and 531 eV, respectively. The Pt 4f-$_{5/2}$ and Pt -4f$_{7/2}$ binding energy of Pt/Ti$_3$ C$_2$T$_x$-CNT in Fig. 1d were 71.93 eV and 74.93 eV, which 0.45 eV and 0.3 eV left shifted from Pt/C, respectively. These shifts indicated a stronger interaction between the Ti-$_3$ C$_2$T$_x$-CNT and Pt nanoparticles than that between carbon and Pt. The peaks of Pt -4f$_{5/2}$ and Pt -4f$_{7/2}$ corresponded to -Pt^0 and -Pt^{2+} peaks, respectively (as shown in Fig. S2 and Table S1), which indicated the formation of the oxidized Pt species.

TEM and HRTEM images as shown in Fig. 2a, b indicated continuous substrates formed by lamellar -Ti$_3$C $_2$T$_x$ and tubular CNTs. Pt nanoparticles were uniformly distributed on the -Ti$_3$C$_2$T$_x$-CNT hybrid support and the Pt particles with a diameter of around 3.36 nm. Figure S1 presents the TEM of layered -Ti$_3$C$_2$T$_x$. Figure 2c exhibits that the fringe spac-ing was around 0.23 nm, which could be recognized as Pt (111) plane in face-centered cubic (fcc) structure. Moreover, the energy-dispersive system (EDS) mapping of the Pt/Ti$_3$C$_2$T$_x$-CNT catalyst in Fig. 2d further confirmed the uniform distribution of characteristic elements, Ti and O in Ti$_3$C$_2$T$_x$, and the C element from both -Ti $_3$C$_2$T $_x$ and CNT. These proved the good dispersibility of Pt nanoparticles on the ultrathin -Ti$_3$C $_2$T$_x$-CNT hybrid support.

As shown in Fig. 3a, b, the solid line indicated the CV and LSV curves for pure H-$_2$ circumstance, and the ECSAs of Pt/Ti$_3$C$_2$T$_x$-CNT and Pt/C catalysts were calculated as 68.65 m^2 g^{-1} and 49.19 m-^{2} g^{-1}, respectively. The Pt/Ti$_3$C$_2$T$_x$-CNT catalysts exhibited a slightly larger ECSA than the Pt/C catalyst. Figure 3 b shows all of the catalysts exhibited the overpotential for H-$_2$ oxidation obviously in pure H-$_2$; the Pt/Ti$_3$C$_2$T$_x$-CNT catalyst provided a higher current den-sity, indicating a higher HOR catalytic activity. A total of 1000 ppm CO with an -H$_2$ mixture was applied to examine the CO tolerance performance of the catalyst; the ECSAs of Pt/Ti$_3$C$_2$T$_x$-CNT and Pt/C catalysts were 65.5 m-^{2} g^{-1} and 41.86 m-^{2} g^{-1}, respectively. The performance decrease of Pt/Ti$_3$C $_2$T $_x$-CNT catalyst (4.6% ECSA lost) is negligible compared to Pt/C (14.9% ECSA lost). Moreover, the limit

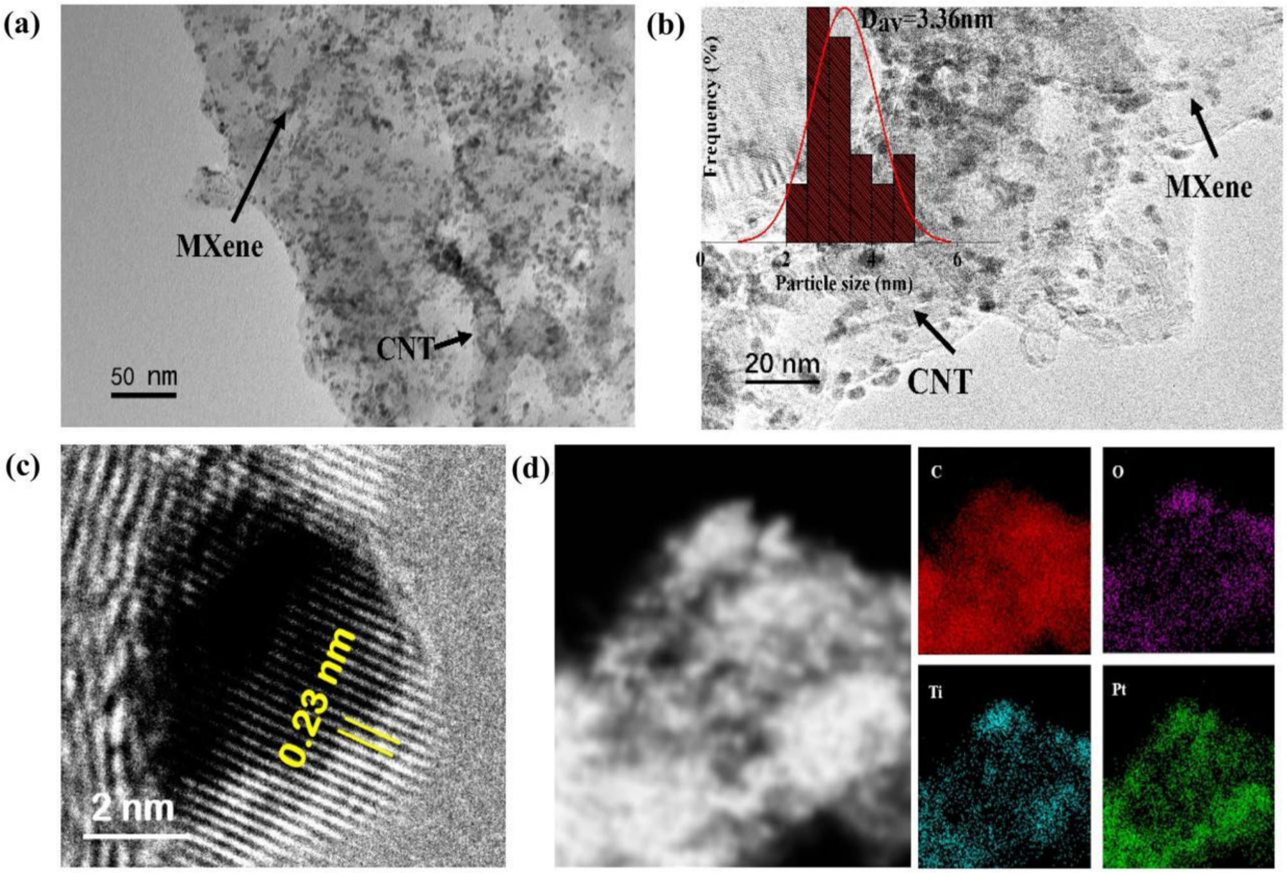

Fig. 2 **a** TEM image of Pt/Ti$_3$C$_2$T$_x$-CNT, **b**, **c** HRTEM image of Pt/Ti$_3$C$_2$T$_x$-CNT, and **d** EDS mapping of Pt/Ti$_3$C$_2$T$_x$-CNT

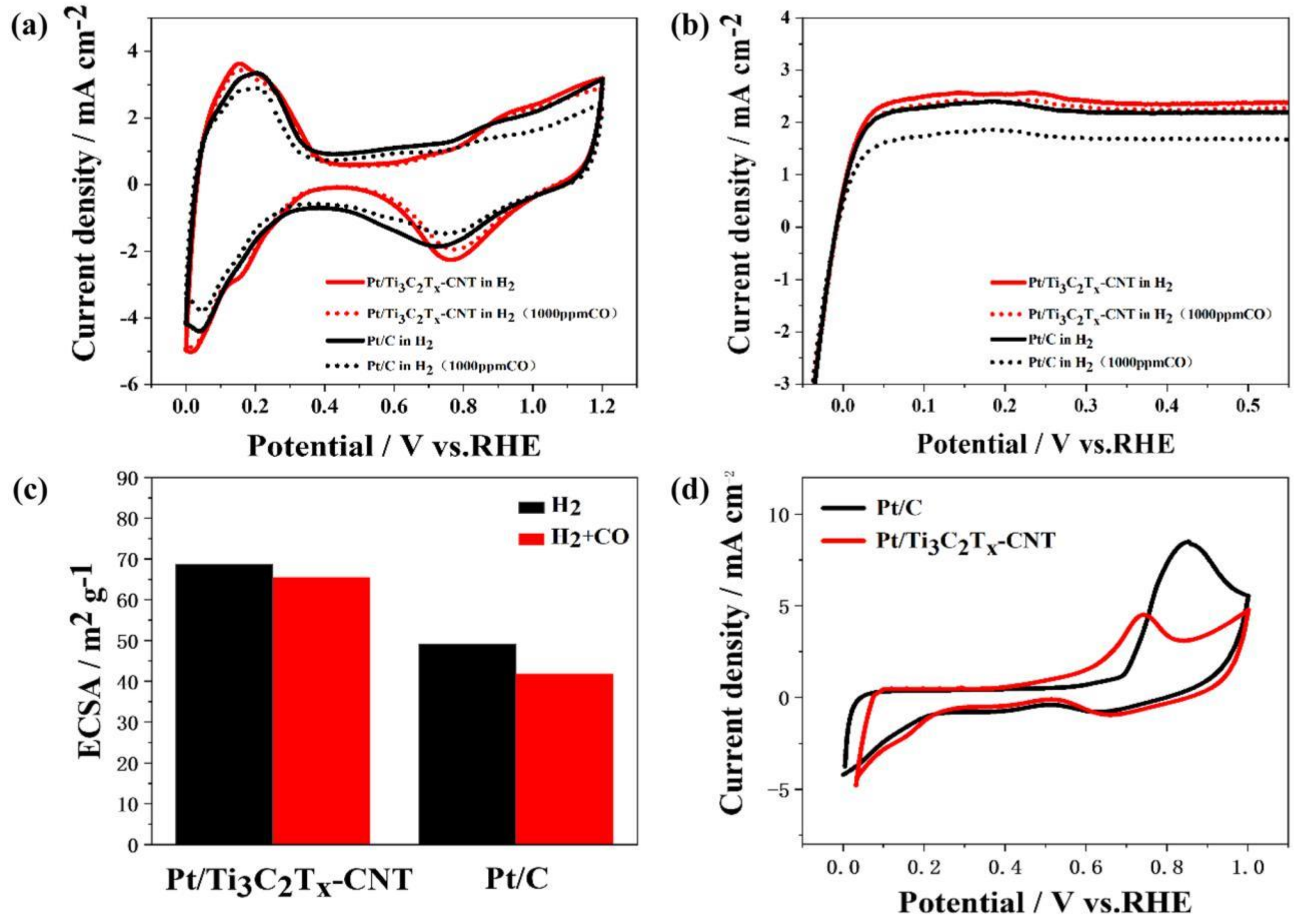

Fig. 3 **a** CV curves for Pt/$Ti_3C_2T_x$-CNT and Pt/C, **b** LSV curves for Pt/$Ti_3C_2T_x$-CNT and Pt/C, **c** The ECSA of Pt/$Ti_3C_2T_x$-CNT and Pt/C, and **d** CO stripping voltammograms of Pt/$Ti_3C_2T_x$-CNT and Pt/C

current of Pt/$Ti_3C_2T_x$ -CNT in Fig. 3b decreased much less than that of Pt/C. As shown in Fig. 3d, the onset potential and the maximum peak for CO oxidation acquired from the Pt/C catalyst are at 0.53 V and 0.85 V, while the onset poten-tial and the maximum peak for CO oxidation are 0.41 V and 0.73 V for Pt/$Ti_3C_2T_x$-CNT catalyst, respectively. These lower values indicate that the Pt/$Ti_3C_2T_x$-CNT catalyst has superior CO oxidation activity than Pt/C because MXene could promote the oxidation of adsorbed CO at lower poten-tials [31–33]. As shown in Fig. S3, it could be seen that an obvious ECSA drop (about 35.6%) of Pt/C catalyst after 1000 cycles of potential sweeping according to the dissolu-tion and sintering of Pt particles and/or the corrosion of the carbon support. However, the Pt/$Ti_3C_2T_x$- CNT catalyst exhibited a smaller ECSA drop; this superior stability may be attributed to the strong interaction between the Pt nano-particles and the Ti-$_3$ C_2T_x-CNT hybrid supports. Moreover, the CNT could also prevent the agglomeration of MXene and reduce the deformation of Pt nanoparticles [34, 35].

As shown in Fig. 4a, the peak power densities of fuel cells based on Pt/$Ti_3C_2T_x$-CNT were 0.86 W with -H_2/Air cm^{-2} and 1.6W cm^{-2} with -H_2/O_2, respectively. The fuel cell based on Pt/$Ti_3C_2T_x$-CNT and commercial Pt/C catalysts both exhibit similar open-circuit voltages (OCVs) with H-$_2$/air in Fig. 4b. Moreover, it can be seen that the current density based on Pt/C anode decreased 29.4% at 0.65 V when CO mixture gas was filled in, while only an 11.1% reduction at 0.65 V based on Pt/ $Ti_3C_2T_x$-CNT anode. Pt/C anode also exhibits larger decay-ing at 0.5 V and 0.8 V than Pt/$Ti_3C_2T_x$-CNT anode in Fig. 4c. These results identified that the Pt/$Ti_3C_2T_x$-CNT catalyst could provide better performance than the commercial Pt/C cata-lyst both in the pure H-$_2$ and CO/H_2 mixture gas. CO-tolerance durability evaluation of the Pt/$Ti_3C_2T_x$-CNT catalysts is dem-onstrated in Fig. 4d. A total of 5 ppm CO/H_2 results in a fast decrease of the relative voltage. The durability was enhanced to over 80 min with the Pt/$Ti_3C_2T_x$-CNT catalyst. These results clearly demonstrate that the Pt/$Ti_3C_2T_x$-CNT catalyst has a much better CO tolerance than that of commercial Pt/C.

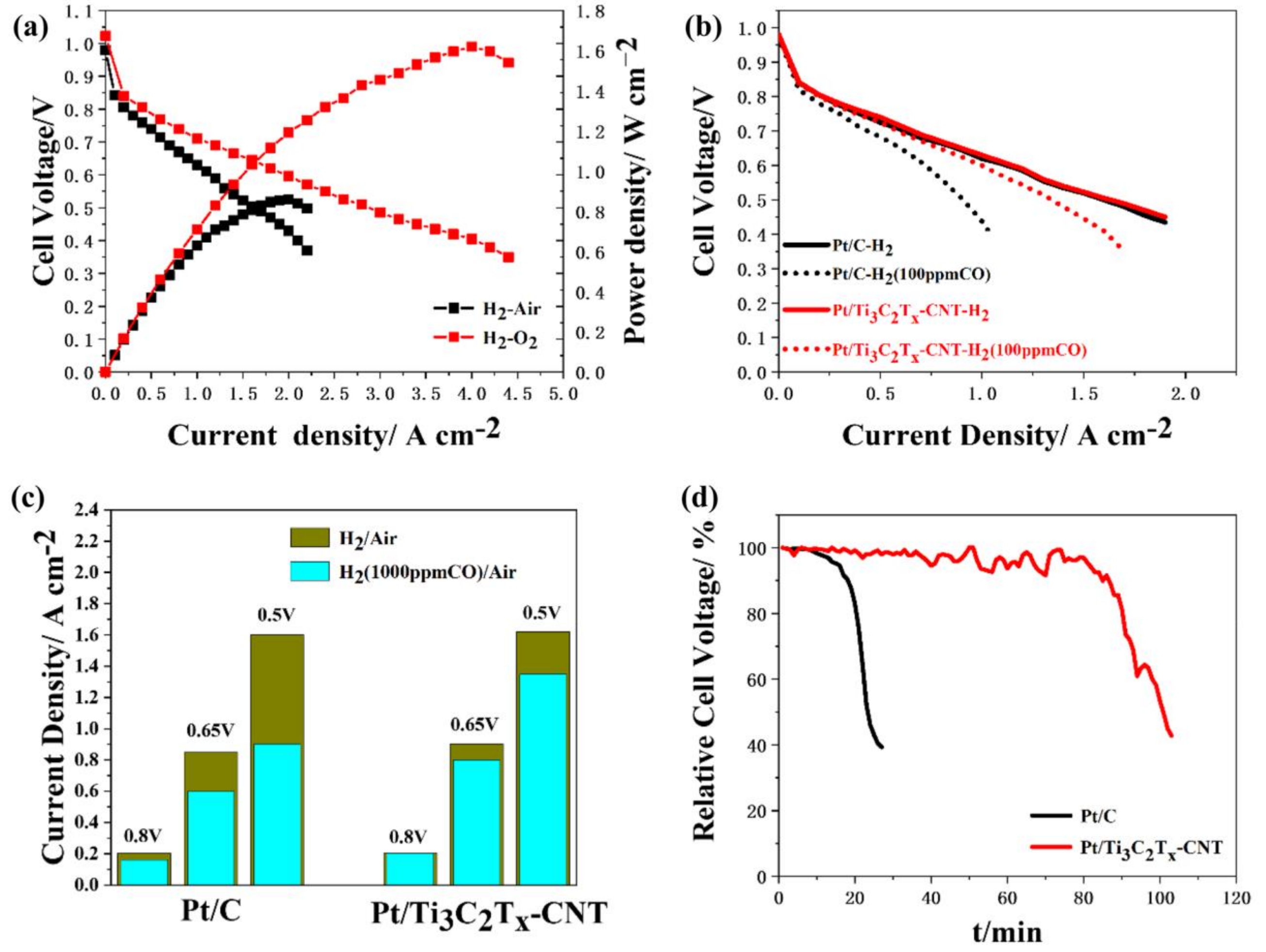

Fig. 4 **a** Polarization curves for MEA (anode: Pt/$Ti_3C_2T_x$-CNT, cathode: Pt/C), **b** polarization curves for Pt/C and Pt/$Ti_3C_2T_x$-CNT as anode catalysts in the presence of 100 ppm CO under -H_2/O_2 conditions, **c** current density for Pt/C and Pt/$Ti_3C_2T_x$-CNT as anode catalysts in different voltages in the presence of 100 ppm CO under H-$_2$/O_2 conditions, and **d** relative voltage vs. time curves of Pt/C and Pt/$Ti_3C_2T_x$-CNT as anode catalysts in the presence of 5 ppm CO at a current density of 0.8A cm-$^{-2}$

Conclusion

In summary, the 2D porous -$Ti_3C_2T_x$-CNT hybrid sup-ports were synthesized by self-assembly of oppositely charged CNT and Ti-$_3C_2T_x$ in an aqueous solution, and the Pt/$Ti_3C_2T_x$-CNT catalyst was obtained by integration of Pt metal and Ti-$_3C_2T_x$ -CNT composite supports through a microwave-assisted polyol reduction method. The Pt/ $Ti_3C_2T_x$-CNT catalyst exhibited higher HOR activities and stability than that of the commercial Pt/C catalyst. The peak power density of Pt/Ti_3C_2 T_x-CNT catalyst achieves 0.86W cm^{-2} with H-$_2$/Air and 1.6 W -cm^{-2} with H- $_2$/O_2, respectively. Moreover, the interactions between Pt nan-oparticles with the -Ti_3 C_2T $_x$-CNT hybrid support could reduce the adsorption of CO to Pt. Pt/Ti_3 C_2T $_x$-CNT catalyst exhibits much less reduction of ECSA and more mitigat-ing fuel cell performance degradation during CO presence.

Funding We thank the financial support from the National Key Research and Development Program of China under Grant No. 2021YFE0191700. We also thank the fund support by Hefei Municipal Natural Science Foundation (2022042).

Declarations

Competing Interests The authors declare no competing interests.

References

\ 1.\ Y.Y. Cong, B.L. Yi, Y.J. Song, Hydrogen oxidation reaction in alkaline media: From mechanism to recent electrocatalysts. Nano Energy **44**, 288–303 (2018)

\ 2.\ V. Mehta, J.S. Cooper, Review and analysis of PEM fuel cell design and manufacturing. J. Power Sources **114**, 32–53 (2003)

\ 3.\ J. Bae, S. Lee, S. Kim, J. Oh, S. Choi, M. Bae, I. Kang, S.P. Katikaneni, Liquid fuel processing for hydrogen production: a review. Int. J. Hydrogen Energy **41**, 19990–20022 (2016)

\ 4.\ A.N. Gennadiev, Y.I. Pikovskii, A.S. Tsibart, M.A. Smirnova, Hydrocarbons in soils: Origin, composition, and behavior (Review). Eurasian Soil Sci. **48**, 1076–1089 (2015)

\ 5.\ A. Basile, F. Dalena, J. Tong, T.N. Veziroğlu, *Hydrogen production, separation and purification for energy*, vol. 89, (IET, 2017)

\ 6.\ G. Voitic, S. Nestl, K. Malli, J. Wagner, B. Bitschnau, F.-A. Mautner, V. Hacker, High purity pressurised hydrogen production from syngas by the steam-iron process. Rsc Adv. **6**, 53533–53541 (2016)

\ 7.\ A.A. Franco, *Polymer electrolyte fuel cells: Science, applications, and challenges* (CRC Press, 2013)

\ 8.\ H. Igarashi, T. Fujino, M. Watanabe, Hydrogen electro-oxidation on platinum catalysts in the presence of trace carbon monoxide. J. Electroanal Chem. **391**, 119–123 (1995)

\ 9.\ N. Zamel, X. Li, Effect of contaminants on polymer electrolyte membrane fuel cells. Prog. Energy Combust Sci. **37**, 292–329 (2011)

\10.\ M. Ahmadi, F. Behafarid, C. Cui, P. Strasser, B. Cuenya, Long-range segregation phenomena in shape-selected bimetallic nanoparticles: chemical state effects *Acs*. NANO **7**, 9195–9204 (2013)

11\.\ J. Li, Z. Luo, F. He, Y. Zuo, C. Zhang, J. Liu, X. Yu, R. Du, T. Zhang, M.F. Infante-Carrió, Colloidal Ni–Co–Sn nanoparticles as efficient electrocatalysts for the methanol oxidation reaction. J. Mater. Chem. A **6**, 22915–22924 (2018)

\12.\ Z. Liu, J.E. Hu, Q. Wang, K. Gaskell, A.I. Frenkel, G.S. Jackson, B. Eichhorn, PtMo alloy and MoO x@ Pt Core− shell nanopar-ticles as highly CO-tolerant electrocatalysts. J. Am. Chem. Soc. **131**, 6924–6925 (2009)

13\.\ Z. Liu, G.S. Jackson, B. Eichhorn, PtSn intermetallic, core–shell, and alloy nanoparticles as CO-tolerant electrocatalysts for H2 oxidation. Angew Chem. Int. Ed. **122**, 3241–3244 (2010)

\14.\ G. Shi, H. Yano, D.A. Tryk, A. Iiyama, H. Uchida, Highly active, CO -tolerant, and robust hydrogen anode catalysts: Pt–M (M= Fe, Co, Ni) alloys with stabilized Pt-skin layers. ACS Catal. **7**, 267–274 (2017)

15\.\ V.R. Stamenkovic, B.S. Mun, K.J. Mayrhofer, P.N. Ross, N. Markovic, Effect of surface composition on electronic structure, stability, and electrocatalytic properties of Pt -transition metal alloys: Pt-skin versus Pt-skeleton surfaces. J. Am. Chem. Soc. **128**, 8813–8819 (2006)

\16.\ J. Svendby, F. Seland, G. Singh, J.L.G. de la Fuente, S. Sunde, The potential of zero total charge and electrocatalytic properties of Ru@ Pt core-shell nanoparticles. J. Electroanal Chem. **833**, 189–197 (2019)

17\.\ B.W. Zhang, Z.C. Zhang, H.G. Liao, Y. Gong, L. Gu, X.M. Qu, L.X. You, S. Liu, L. Huang, X.C. Tian, R. Huang, F.C. Zhu, T. Liu, Y.X. Jiang, Z.Y. Zhou, S.G. Sun, Tuning Pt-skin to Ni- rich surface of Pt3Ni catalysts supported on porous carbon for enhanced oxygen reduction reaction and formic electro-oxidation. Nano Energy **19**, 198–209 (2016)

\18.\ K.-W. Park, J.- H. Choi, B.-K. Kwon, S.-A. Lee, Y.-E. Sung, H.-Y. Ha, S.-A. Hong, H. Kim, A. Wieckowski, Chemical and electronic effects of Ni in Pt/Ni and Pt/Ru/Ni alloy nanoparticles in methanol electrooxidation. J. Phys. Chem. B **106**, 1869–1877 (2002)

19\.\ K. Singh, E.B. Tetteh, H.-Y. Lee, T.-H. Kang, J.-S. Yu, Tailor-made Pt catalysts with improved oxygen reduction reaction stability/durability. ACS Catal. **9**, 8622–8645 (2019)

\20.\ Y. Wang, G. Wang, G. Li, B. Huang, J. Pan, Q. Liu, J. Han, L. Xiao, J. Lu, L. Zhuang, Pt–Ru catalyzed hydrogen oxidation in alkaline media: Oxophilic effect or electronic effect? Energy Environ. **8**, 177–181 (2015)

21\.\ L. Lin, S. Yao, R. Gao, X. Liang, Q. Yu, Y. Deng, J. Liu, M. Peng, Z. Jiang, S. Li, A highly CO-tolerant atomically dispersed Pt catalyst for chemoselective hydrogenation. Nat. Nanotechnol. **14**, 354–361 (2019)

22\.\ R.M. Antoniassi, J. Quiroz, E. Barbosa, L.S. Parreira, R.A. Isidoro, E. Spinace, J. Silva, P.H. Camargo, Improving the electrocatalytic activities and CO tolerance of Pt NPs by incorporating TiO2 nanocubes onto carbon supports. ChemCatChem **13**, 1931–1939 (2021)

23\.\ Y. Wang, D. Widmann, M. Heenemann, T. Diemant, J. Biskupek, R. Schloegl, The role of electronic metal-support interactions and its temperature dependence: CO adsorption and CO oxidation on Au/TiO2 catalysts in the presence of TiO-$_2$ bulk defects. J. Catal. **354**, 46–60 (2017)

24\.\ W. Bao, L. Liu, C. Wang, S. Choi, D. Wang, G. Wang, Solar cells: Facile synthesis of crumpled nitrogen-doped MXene nanosheets as a new sulfur host for lithium–sulfur batteries. Adv. Energy Mater. **8**, 1870060 (2018)

\25.\ C. Chen, X. Xie, B. Anasori, A. Sarycheva, T. Makaryan, M. Zhao, P. Urbankowski, L. Miao, J. Jiang, Y. Gogotsi, MoS2-on-MXene heterostructures as highly reversible anode materials for lithium-ion batteries. Angew Chem. Int. Ed. **57**, 1846–1850 (2018)

\26.\ M.R. Lukatskaya, O. Mashtalir, C.E. Ren, Y. Dall'Agnese, P. Rozier, P.L. Taberna, M. Naguib, P. Simon, M.W. Barsoum, Y. Gogotsi, Cation intercalation and high volumetric capacitance of two-dimensional titanium carbide. Science **341**, 1502–1505 (2013)

27\.\ F. Shahzad, M. Alhabeb, C.B. Hatter, B. Anasori, S.M. Hong, C.M. Koo, Y. Gogotsi, Electromagnetic interference shield-ing with 2D transition metal carbides (MXenes). Science **353**, 1137–1140 (2016)

\28.\ S.H. Talib, S. Baskaran, X. Yu, Q. Yu, B. Bashir, S. Muhammad, S. Hussain, X. Chen, J. Li, Non-noble metal single-atom catalyst of Co 1/MXene (Mo 2 CS 2) for CO oxidation. Sci. China Mater. **64**, 651–663 (2021)

29\.\ X. Wang, S. Kajiyama, H. Iinuma, E. Hosono, S. Oro, I. Moriguchi, M. Okubo, A. Yamada, Pseudocapacitance of MXene nanosheets for high-power sodium-ion hybrid capacitors. Nat. Commun. **6**, 1–6 (2015)

\30.\ Z. Li, Y.R. Cui, Z.W. Wu, C. Milligan, L. Zhou, G. Mitchell, B. Xu, E.Z. Shi, J.T. Miller, F.H. Ribeiro, Y. Wu, Reactive metal-support interactions at moderate temperature in two-dimensional niobium-carbide-supported platinum catalysts. Nat. Cata. **1**, 349– 355 (2018)

\31.\ C. Cheng, X. Zhang, M. Wang, S. Wang, Z. Yang, Single Pd atomic catalyst on Mo 2 CO 2 monolayer (MXene): Unusual activity for CO oxidation by trimolecular Eley- Rideal mechanism. Phys. Chem. Chem. Phys. **20**, 3504–3513 (2018)

32\.\ C. Cheng, X. Zhang, Z. Yang, K. Hermansson, Identification of high-performance single-atom Mxenes catalysts for low-temperature CO oxidation. Adv. Theory Simul. **2**, 1900006 (2019)

\33.\ C. Cheng, X. Zhang, Z. Yang, Z. Zhou, Cu3-cluster- doped mon-olayer Mo2CO2 (MXene) as an electron reservoir for catalyz-ing a CO oxidation reaction. ACS Appl. Mater. Interfaces **10**, 32903–32912 (2018)

34\.\ X. Xie, M.-Q. Zhao, B. Anasori, K. Maleski, C.E. Ren, J. Li, B.W. Byles, E. Pomerantseva, G. Wang, Y. Gogotsi, Porous heterostructured MXene/carbon nanotube composite paper with high volumetric capacity for sodium-based energy storage devices. Nano Energy **26**, 513–523 (2016)

\35.\ C.X. Xu, C.C. Fan, X.L. Zhang, H.T. Chen, X.T. Liu, Z.M. Fu, R.R. Wang, T. Hong, J.G. Cheng, MXene (Ti3C2Tx) and carbon nanotube hybrid-supported platinum catalysts for the high-performance oxygen reduction reaction in PEMFC. ACS Appl. Mater. Interfaces **12**, 19539–19546 (2020)

36\.\ M. Alhabeb, K. Maleski, B. Anasori, P. Lelyukh, L. Clark, S. Sin, Y. Gogotsi, Guidelines for synthesis and processing of two-dimensional titanium carbide (Ti3C2T x MXene). Science **29**, 7633–7644 (2017)